Metre-scale damage zone characterization using *S*-coda waves from active ultrasonic transmission measurements in the STIMTEC project, URL Reiche Zeche, Germany

Aglaja Blanke [ORCID],[1] Carolin M. Boese,[1] Georg Dresen,[1] Marco Bohnhoff [ORCID][1,2] and Grzegorz Kwiatek[1]

[1]*GFZ German Research Centre for Geosciences, Section* 4.2: *Geomechanics and Scientific Drilling, Telegrafenberg, D-14473 Potsdam, Germany.*
E-mail: *a_blanke@gfz-potsdam.de*
[2]*Department of Earth Sciences, Free University Berlin, Malteserstraße* 74-100, *D-12249 Berlin, Germany*

SUMMARY

Studies of controlled hydraulic stimulation experiments with active and passive seismic monitoring conducted in Underground Research Laboratories (URLs) benefit from specific knowledge of hydraulic parameters, close by microseismic monitoring revealing structural details of the rock mass, and detailed evolution of seismicity in response to injection operations. Microseismic monitoring is commonly used to characterize a stimulated reservoir volume, for example, in terms of damage evolution of the rock mass. Since seismic attenuation is affected by damage of the rock volume, active seismic sources covering sizes from the centimetre to decimetre scale may help us to investigate space–time varying attenuation properties in a reservoir. This may allow us to monitor damage evolution of the stimulated rock volume in more detail, also since active seismic sources produce stronger signals leading to a broader frequency range that can be analysed compared to passive seismic signals. Within the STIMTEC project in the URL Reiche Zeche (URL-RZ) in Freiberg (Germany), more than 300 active Ultrasonic Transmission (UT) measurements were performed before and after hydraulic stimulations in two boreholes in the targeted rock volume, an anisotropic metamorphic gneiss. The signal-frequency content ranges between 1 and 60 kHz. Assuming scattering attenuation to dominate over intrinsic attenuation, we here apply the single isotropic scattering model. *S*-coda waves of 88 spatially representative UT measurements are used to estimate the coda quality factor (Q_C). We obtain stable Q_C estimates for centre frequencies of octave-width frequency bands between 3 and 21 kHz. We group neighbouring UT measurements to stabilize the observations and form eight UT groups in total, covering different depth intervals in three boreholes and four different time periods to investigate scattering attenuation changes in a spatiotemporal manner. Our final mean Q_C ($\overline{Q_C}$) estimates show characteristic frequency-dependence as observed at the field scale in geological reservoirs. We find temporal variations of Q_C are strongly connected to hydraulic stimulation, and these variations are more significant than those resolved from velocity changes. $\overline{Q_C}$ estimates at frequencies above 15 kHz indicate healing of injection-induced small-scale fractures during a two-months post-stimulation phase. Larger fractures, mostly sampled by lower frequencies (<15 kHz), seem to be more persistent with time (over 15 months). We observe spatial differences of $\overline{Q_C}$ values near the mine galleries (driftway and vein drift) and relate these observations to different extents and characteristics of the galleries' excavation damage zones. Our results further support previous assumptions based on borehole televiewer logs and mapped structures of an existing fault with larger damage zone that crosses the stimulated rock volume NW-SE between the galleries. We conclude that the coda analysis of active UT measurements complements established imaging methods used during experiments in URLs. In particular, coda analysis is a powerful tool for the detection of damage zones and for monitoring local fracture networks with immediate application for imaging georeservoirs considered for exploitation or underground storage of gases and liquids.

1 INTRODUCTION

The Earth's upper crust is characterized by complexity with inhomogeneities at multiple length scales (e.g. Holliger 1996; Sato *et al.* 2012). Particularly when analysing small earthquakes at the field- (magnitude $M < 4$), the meso- ($M < -1$) or the laboratory scale ($M < -4$), structural features, pore-fluids and mineral grain size may all have a strong impact on high-frequency seismic waves during their propagation from source to receiver (e.g. Aki & Chouet 1975; Abercrombie 1995; Winkler & Murphy 1995; Adams & Abercrombie 1998). This leads to extensive variation in recorded amplitudes of seismic waves, their frequency content and coda wave duration over short distances (e.g. Abercrombie 1998, 2000; Calvet *et al.* 2013). These effects, when not accounted for, may bias the analysis of seismic source characteristics such as stress drop or apparent stress and lead to discrepancies between individual studies (e.g. Ide *et al.* 2003; Abercrombie 2015, 2021; Shearer *et al.* 2019). For any in-depth study of seismic source parameters, it is therefore essential to quantify and consider uncertainties during recording and processing of seismic waveform data, and properly account for attenuation effects.

Experiments on rock samples in the laboratory or *in-situ* seismic measurements in URLs can provide valuable input for the study of small earthquakes (source sizes from sub-mm to 100 m). This is because key parameters such as loading conditions, fluid injection volume and rock properties are known and, moreover, some can be modified when needed. Furthermore, by using active seismic signals (i.e. UT signals), waveforms have known characteristics and are generated at known locations. These facilitate, for instance, a closer investigation of seismic source parameters and their natural variability. Furthermore, the analysis of waveforms originating from source sizes at the centimetre to decimetre scale from active or passive seismic campaigns help us to decipher the role of attenuation and its impact on high-frequency seismic waves. Investigating attenuation may also provide key information for detecting and imaging damage zones, fracture networks and areas with high fracture density, providing relevant data for reservoir exploitation and underground storage of gases and liquids (e.g. Obermann *et al.* 2015; Zhu *et al.* 2017, 2019).

Apart from geometrical spreading, energy of seismic waves decays due to intrinsic and scattering attenuation, which are difficult to separate from each other using the seismic data. The quality factor Q depicts a combined effect of intrinsic and scattering attenuation processes (e.g. Gibowicz and Kijko 1994 ; Frankel & Wenneberg 1987) and is typically used to correct raw seismic signals for attenuation. Intrinsic attenuation (Q_i) is the result of inelastic energy loss primarily due to viscous damping from local pore fluid motion and grain boundary effects. Q_i increases as permeability, fluid pressure or fluid viscosity increase (Johnston *et al.* 1979; Winkler & Murphy 1995). Scattering attenuation (Q_{sc}) results from reflection, refraction and diffraction processes predominantly at small-scale heterogeneities such as faults and cracks (e.g. Aki 1969; Sato *et al.* 2012). As seismic waves pass through heterogeneous rock, elastic seismic energy is redistributed in space and time reducing wave amplitudes and causing late arrivals of incoherent wave portions in the seismogram known as coda waves (e.g. Aki 1969, 1980b; Sato *et al.* 2012). Thus, coda waves spend more time in the investigated rock volume than direct waves and contain important information on the structural complexity of a reservoir (e.g. Blanke *et al.* 2019).

At the field scale, several different coda analysis methods are applied to estimate attenuation of coda waves, coda Q (Q_C), typically within frequency ranges between 1 and 30 Hz (e.g. Aki 1980a; Phillips *et al.* 1988; Novelo-Casanova & Lee 1991; Gibowicz & Kijko 1994; Mukhopadhyay *et al.* 2008; Calvet & Margerin 2013; Wang & Shearer 2018). Investigations show that intrinsic attenuation is the dominant process in this frequency range (e.g. Sato *et al.* 2012). Higher frequencies up to 70–160 Hz were studied to a lesser extent only (e.g. Leary & Abercrombie 1994; Blanke *et al.* 2019). Field studies suggest that scattering effects become more relevant in the crust at higher frequencies (>10 Hz) than it is the case at lower frequencies (e.g. Leary & Abercrombie 1994). High-frequency waves exhibit more oscillations in space and with time and are therefore more sensitive to obstacles (scatterers), and thus scattering leads to increasing Q_C values with increasing frequency (frequency-dependency). The proportion between intrinsic and scattering attenuation at high frequencies is difficult to determine and up to date not well investigated.

Little is known about the impact of attenuation on seismic waves at even higher frequencies as observed in laboratory and URL experiments. At the laboratory scale, for instance, only a limited number of recent studies exist that investigate attenuation of active ultrasonic measurements (0.1–1 MHz) in laboratory rock samples (e.g. Guo *et al.* 2009; Wei & Fu 2014; Hu *et al.* 2017; Ma & Ba 2020). It is assumed that scattering is strong as lengths of inhomogeneities (e.g. faults, microfractures and grain sizes) and analysed wavelengths are similar and possibly interact with each other. The single isotropic scattering model was used by Guo *et al.* (2009) and Hu *et al.* (2017) to estimate Q_C during a triaxial rock deformation experiment (frequencies ranging 0.4–0.9 MHz) and a uniaxial rock deformation experiment (0.3–1.2 MHz), respectively. In both studies, S-wave Q_C estimates increase slightly at lower frequencies, then show a peak at ~0.7 MHz and again decrease towards higher frequencies. The inconsistency of increasing and decreasing Q_C values at very high frequencies at the laboratory scale is contrary to observations from field studies. A comparative study of a multiple-scattering model applied on same rock specimens by Hu *et al.* (2017) indicates that Q_C shows a similar behaviour like the single scattering model and thus the model assumption seems to be independent from the laboratory Q_C estimate observations. In general, coda wave analysis is considered to be an effective tool to characterize attenuation of laboratory seismic signals. However, attenuation studies may be affected by reflections caused by the limited size of lab test specimens.

Only few Q_C studies exist of experiments performed in URLs. Plenkers *et al.* (2009) analysed Q_C values of S-coda waves from nano- and picoseismicity in the Mponeng Deep Gold Mine in South Africa ($M = -5$ to -1) using the single isotropic scattering model. In the range between 25 and 145 kHz, frequency-dependent Q_C estimates of 100–600 were obtained that are comparable to field scale observations. The Q_C results at low frequencies were compatible to frequency-independent Q estimates estimated from direct phases (Kwiatek et al. 2011). Krauß *et al.* (2014) used direct P-wave information of a vibrator source (signal frequency range: ~0.15–3 kHz) to assess spatial Q_P variations in the underground GFZ laboratory at the URL-RZ in Freiberg (Germany), which is 180 m north of the SIMTEC project site. The authors found that estimated Q_P values from damage zones are reduced by up to 10 per cent compared to P-wave velocity reduction by only 2 per cent. This observation

suggests that seismic wave attenuation reacts more sensitive to rock damage variations than seismic velocity measurements. In contrast to Q of direct phases that are limited to the respective frequency bands, attenuation analysis of coda waves covers a broad range of frequencies within a rock volume and thus may provide more detailed information on fracture sizes and density.

In this study, we aim at analysing high-frequency active UT recordings (1–60 kHz) to characterize attenuation properties at the STIMTEC project site in the URL-RZ, where a series of mesoscale hydraulic stimulation experiments were performed (e.g. Boese *et al.* 2022). There are several advantages of using UT measurements. The UT source signal is clearly defined, repetitive and stable in a wide frequency range in contrast to passive seismic signals that are typically used to assess the scattering properties at the field scale. Considering the analysed frequency range of measured UT signals with wavelengths (λ) of approx. 0.16–1.6 m, we expect strong influence of scattering attenuation on the high-frequency records. Intrinsic attenuation in the STIMTEC project site is most likely caused by dominant rock features, which is foliation of the gneiss in the investigated rock volume. Tiny structural features make up the foliation as shown by Adero (2020) which plays an important role at the laboratory scale. The frequency range and wavelengths of analysed UT measurements, however, are assumed to interact with small-scale inhomogeneities of the order of joints and faults, but also the rock saturation state, and lithologic variations (e.g. Sato 1977) which likely affect the measured UT signals the most. Thus, similar to lab experiments but at a larger scale, we assume scattering to be dominant due to the interaction of UT wavelengths and structures of centimetre-to-decimetre scale (e.g. Sato *et al.* 2012). Furthermore, we investigate, how much the local fracture network in the vicinity of the injection points and thus wave scattering attenuation processes are modified transiently or semipermanently by hydraulic stimulation. Therefore, we analyse spatiotemporal changes in the coda amplitude decay of high-frequency UT measurements before and after injection phases in the STIMTEC project. We use the single isotropic scattering model applied to the early *S*-wave coda at short source-to-receiver distances (<30 m) following the approach of Phillips (1985). Finally, we assess our observations from the URL scale and discuss the relevance of the study outcome for applications at larger scales and in reservoir exploitation and exploration.

2 THE STIMTEC EXPERIMENTAL SETUP

Between 2018 and 2019, the STIMTEC hydraulic stimulation experiment was conducted at the URL-RZ in Freiberg (Germany) at a depth of about 130 m below surface in strongly foliated metamorphic gneiss. This experiment was designed to investigate the role of stimulation processes in enhancing hydraulic properties of crystalline rocks (e.g. Renner & STIMTEC team 2021; Boese *et al.* 2022). The STIMTEC experiment comprised several phases of stimulation, hydraulic testing and validation, during which active and passive seismic measurements were acquired to investigate elastic velocity changes, and to observe correlations between damage patterns, hydraulic stimulation and seismic activity (e.g. Jimenez-Martinez & Renner 2021; Boese *et al.* 2022).

Two galleries, a straight driftway and a curved vein drift (Fig. 1a), surround the monitored rock volume with dimensions of 40 m × 50 m × 30 m. The galleries were excavated in 1903 (vein drift) and 1950 (driftway), likely resulting in different widths of the excavation damage zone. Some 180 m north of the STIMTEC project site along the same galleries (e.g. Giese & Jaksch 2016), Krauß *et al.* (2014) have reported an excavation damage zone extending up to 10 m

into the rock volume with an estimated 7 per cent reduction in *P*-wave velocity based on active seismic measurements. During the STIMTEC project, six boreholes (BH09, BH10, BH12, BH15, BH16 and BH17) with different and mostly downward dipping orientations were drilled into the stimulated rock volume from both galleries and used for active measurements (Figs 1a and b). A high-sensitivity seismic network composed of Acoustic Emission (AE) sensors, high-frequency accelerometers and a broad-band sensor was installed in shorter and mainly upward trending boreholes that cover the rock volume from above and are used to monitor high-frequency (>1 kHz) active UT signals and passive AE activity (see Boese *et al.* 2022 for details).

Hydraulic stimulations were conducted in borehole BH10 during the stimulation phase (2018 July 16–18) and in the vertical borehole BH17 during the validation phase (2019 August 21–22). Over the course of the stimulation phase in 2018, water was injected in ten different intervals between 22.4 and 56.5 m borehole depth in BH10. The injected volumes varied from approx. 55 to 460 litres (*cf.* table 2 of Boese *et al.* 2022). These stimulations resulted in the occurrence of AE events during the injection in the shallow part of the borehole, highlighting the activation or reactivation of fracture network at the decimetre scale (*cf.* fig. 5 of Boese *et al.* 2022). During the validation phase in 2019, water was injected in five intervals into borehole BH17, a vertical borehole in the driftway which is 10 m distant to BH16. Only a small amount of water (18–33 litres) was injected into each interval. The largest number of injection-induced AE events during the validation phase occurred between boreholes BH17 and BH16.

In this study, we focus on 88 selected out of >300 active UT measurements from boreholes BH10, BH12 and BH16 (black dots in Fig. 1a). Boreholes BH10 and BH16 run subparallel about 4.5 m apart and dip approx. 15° downwards. BH12 has a dip of 36° from the driftway and crosses BH10 and BH16 below at approx. 33.9 and 18 m borehole depth, respectively. Acoustic televiewer images from both boreholes and cores reveal multiple fractures in borehole BH10 between 42 and 47 m depth and between 34 and 40 m depth in borehole BH16 (Fig. 1b). In these zones, a significant reduction in seismic velocity by up to 300 m s^{-1} and seismic background anisotropy was observed (*cf.* fig. S8a of Boese *et al.* 2022). Anisotropy originates from the sub-horizontal foliation of the gneiss but is weaker in zones of increased fracture density. Due to inaccuracy of the derived velocity model in these damage zones, AE events exhibit increased location errors (*cf.* figs 4 and 8 of Boese *et al.* 2022). Furthermore, structural markers along both galleries indicate zones of enhanced damage due to faulting (Fig. 1a). If and how these damage zones are connected between both galleries, as indicated by detected fractures in BH10 and BH16, remains unclear. Adero (2021) measured *P*-wave velocities in the laboratory, using cylindrical Freiberger gneiss samples at different orientations at room temperature and showed that seismic wave attenuation perpendicular to the foliation is significantly larger than parallel to the foliation.

3 DATA

More than 300 UT measurements (Fig. 1) were available to verify and better characterize observations of reduced velocity and fracture density indicating zones of enhanced damage and increased attenuation in the mine (e.g. Adero 2021; Boese *et al.* 2022). Active source UT signals were produced by an ultrasonic transmitter (central frequency $\sim$ 15 kHz) that discharges a delta source time pulse. A total of 1024 pulses were automatically stacked to improve the signal-to-noise ratio (SNR) at each AE sensor. The UT signals
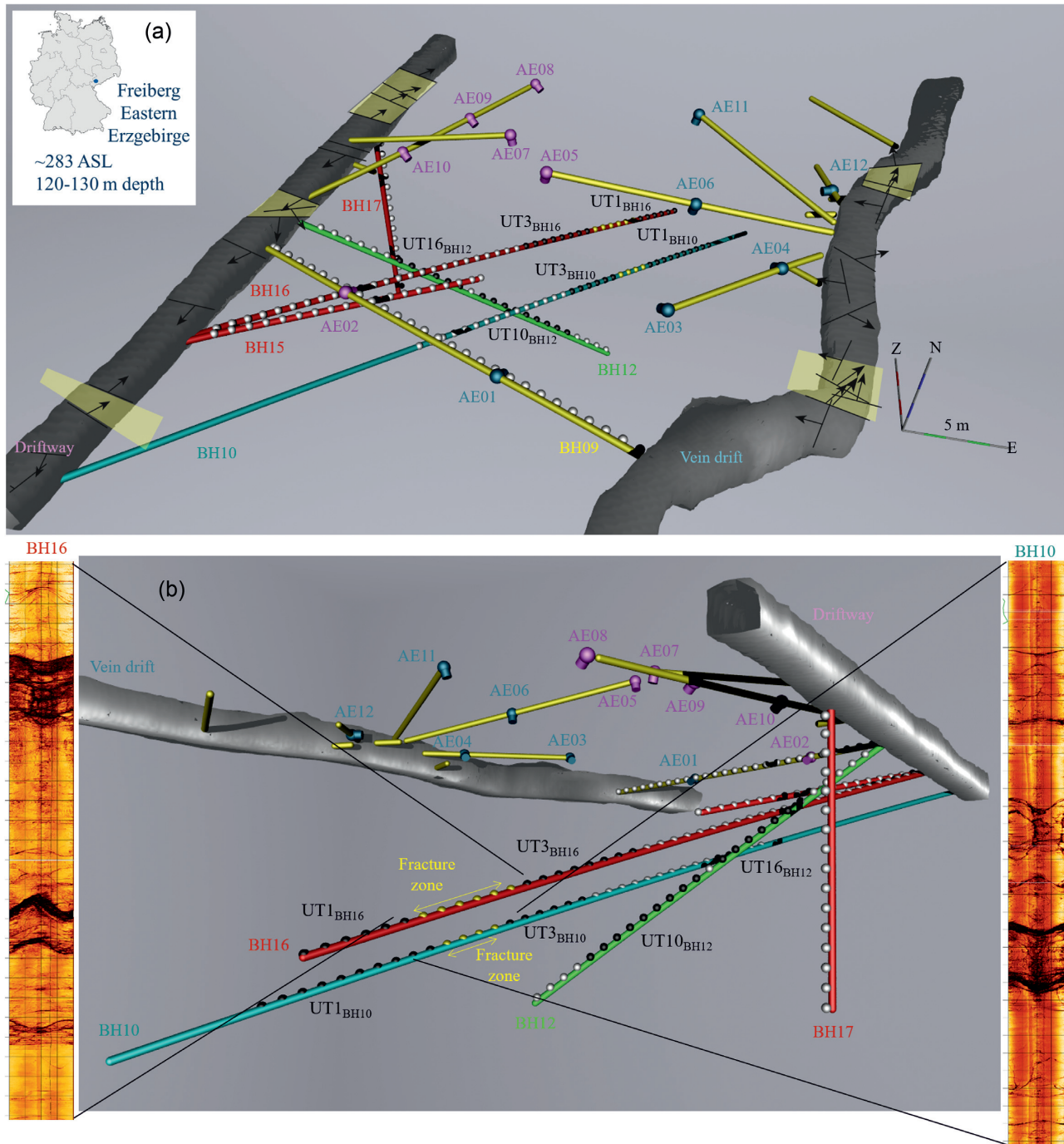
Figure 1. Overview of the borehole and sensor network at the URL-RZ. The 40 m × 50 m × 30 m rock volume of interest is situated between the curved eastern gallery (vein drift) and the straight western gallery (driftway). The monitoring system comprises twelve AE sensors (magenta and turquoise) located in horizontal or upwards going seismic monitoring boreholes (yellow). (a) The perspective view (looking approx. north) indicates positions of ultrasonic transmitter (UT) source signals in all boreholes (dots along boreholes). The yellow-coloured dots indicate the damage zone identified by acoustic borehole televiewer logs in BH10 and BH16. The black dots in BH10, BH16 and BH12 indicate selected UT signal groups used in the final coda analysis. Inset shows the regional setting of the mine in Freiberg, Germany. (b) Side view (looking SE) of the URL. Acoustic borehole televiewer logs of BH10 and BH16 are displayed at the sides showing prominently fractured sections identified in the injection (BH10) and long validation (BH16) boreholes (*cf.* fig. 2 of Boese *et al.* 2022).

cover a frequency band of approximately 1–60 kHz. The UT signals display typical coda lengths <20 ms duration at the AE sensors. In this study, we spatially selected 88 UT measurements from boreholes BH10, BH16 and BH12 to perform the coda analysis.

UT measurements from borehole BH10 were acquired one month before and 1–2 d after the stimulation phase in 2018. UT measurements in borehole BH16 were conducted 1 d after the stimulation of BH17 during the validation phase in 2019 (Boese *et al.* 2022). These data are used to determine the spatial elastic anisotropy in the mine and to identify local high-attenuation deformation zones in the rock volume. Additional UT measurements in borehole BH12 were acquired 2 months after the validation phase
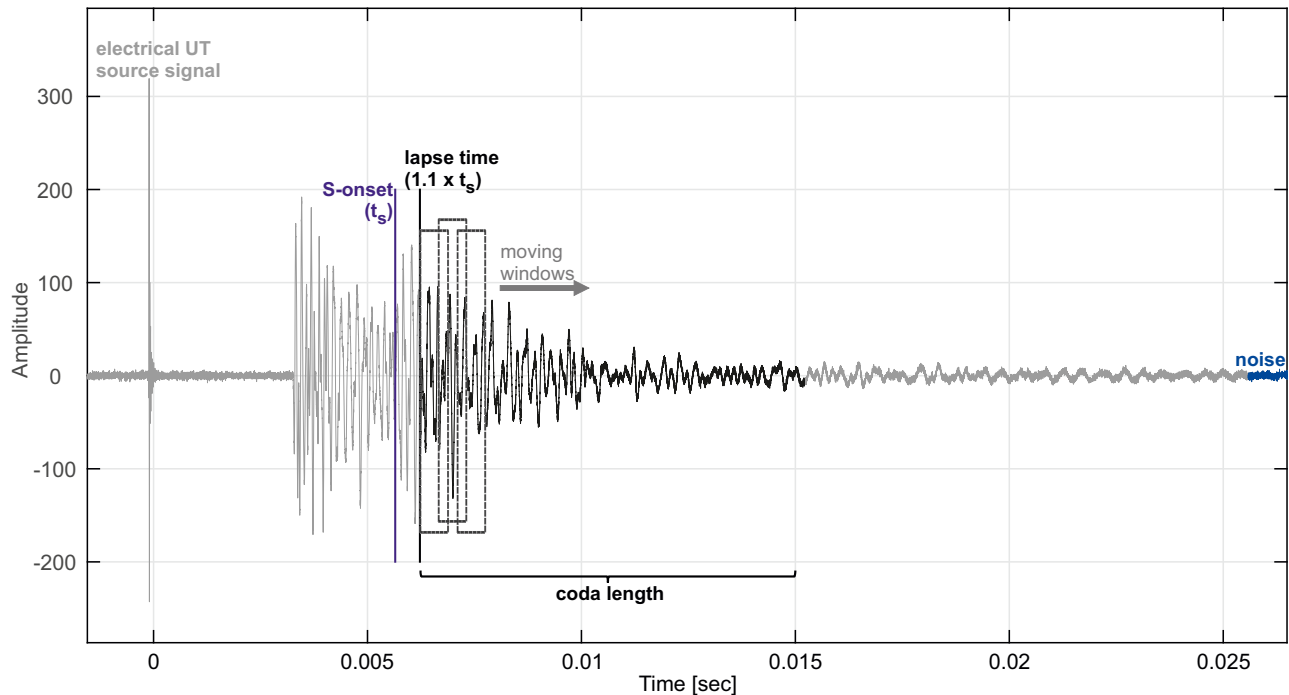
Figure 2. Stacked and filtered UT measurement at one AE sensor. At the zero mark an electric pulse caused by the transmitter of the UT source signal is seen, marking the origin time. The lapse time marker follows the *S*-onset time marker after $1.1 \times t_s$. Moving windows are defined and overlap by 40 per cent to guarantee uncorrelated residuals (Phillips & Aki 1986). The coda length of 9 ms is defined by waveform records at most distant sensors. A reference noise signal is taken from the very end of the seismogram.

and analysed and compared to data from BH10 and BH16 to extend the investigation of temporal attenuation changes before and after hydraulic stimulation periods.

The high-frequency UT signals were recorded using a 16 sensors monitoring network, comprising 12 piezoelectric AE sensors, three accelerometers and one borehole broad-band seismometer (Boese *et al.* 2022). For the coda analysis, we only use the AE sensors that are *GMuG∗ MA BLw-7–70-75* AE side-view 1-component sensors sensitive within a frequency range of 1–100 kHz. The accelerometers and broad-band sensor were found to be too insensitive and band-limited to capture the high-frequency UT signals at the given source-to-receiver distances, thus they were not used in this study. The UT signals were recorded using a 16-bit acquisition system in triggered mode with a 1 MHz sampling frequency. For analysis purposes, we differentiate AE sensors located closer to the vein drift (AE01, AE03, AE04, AE06, AE11, AE12; colour-coded in turquoise in Fig. 1a) and sensors closer to the driftway (AE02, AE10, AE07, AE05, AE09, AE08; colour-coded in magenta in Fig. 1a).

Seismic *P*- and *S*-wave velocities, manually picked *P*- and *S*-arrival times and the origin time of the UT source signals were taken from Boese *et al.* (2021). For the *S*-wave coda analysis at least *P*-wave picks are required. Using the velocity information, missing *S*-wave picks could be calculated to achieve information on the approximate start of the *S*-wave coda. Due to the use of high frequencies, the SNR is relatively low, limiting the reliable frequency range considered in the coda analysis (*cf.* Fig. S1, Supporting Information). In the following, we estimate the coda quality factor (Q_C) for predefined octave-width frequency bands with centre frequencies between 1.5 and 40 kHz.

∗Gesellschaft für Materialprüfung und Geophysik (www.gmugmbh.de), last accessed 2022 December.

4 METHOD

We applied the coda analysis technique of Phillips (1985) to estimate the frequency-dependent Q_C for each UT measurement point at each AE sensor. The method assumes a single isotropic scattering model, in which a point source is spatially separated from the receiver, and inhomogeneities are randomly but homogeneously distributed in the medium. The close distance between source and receiver allows us to start the analysis early in the *S*-wave coda (Sato 1977) and not, like in other methods, only after two times the *S*-wave onset time t_s (e.g. Rautian & Khalturin 1978). This is important because due to the high-frequency content, typically the coda of UT signals is short (< 20 ms) and exhibits a low SNR in the later coda portion. The method assumes the seismic coda consists mainly of scattered *S* waves at short distances (e.g. Aki & Chouet 1975; Aki 1980b, 1981). The scattering mechanism becomes stronger, when inhomogeneities and wavelengths are of similar size (e.g. Sato *et al.* 2012). The applied technique comprises two parts, the moving window analysis and a subsequent regression analysis to obtain Q_C.

4.1 Moving window analysis

To decide on suitable lengths of the moving analysis windows, lapse time and coda window, we followed the results of the sensitivity analysis of Blanke *et al.* (2019). We used a moving window length of 1024 samples to guarantee enough wave oscillations of the signal in each window. The lapse time was fixed to $1.1 \times t_s$ to exclude effects (e.g. radiation pattern, directivity effects) of the direct *S* wave, and we constrained the analysed coda length to 9000 samples (9 ms) to have the same coda length investigated at all sensors (Fig. 2) as at more distant sensors the noise level is reached faster than at close sensors. To assure the use of coda signals clearly above the noise (SNR = 2), a reference noise level for the coda analysis
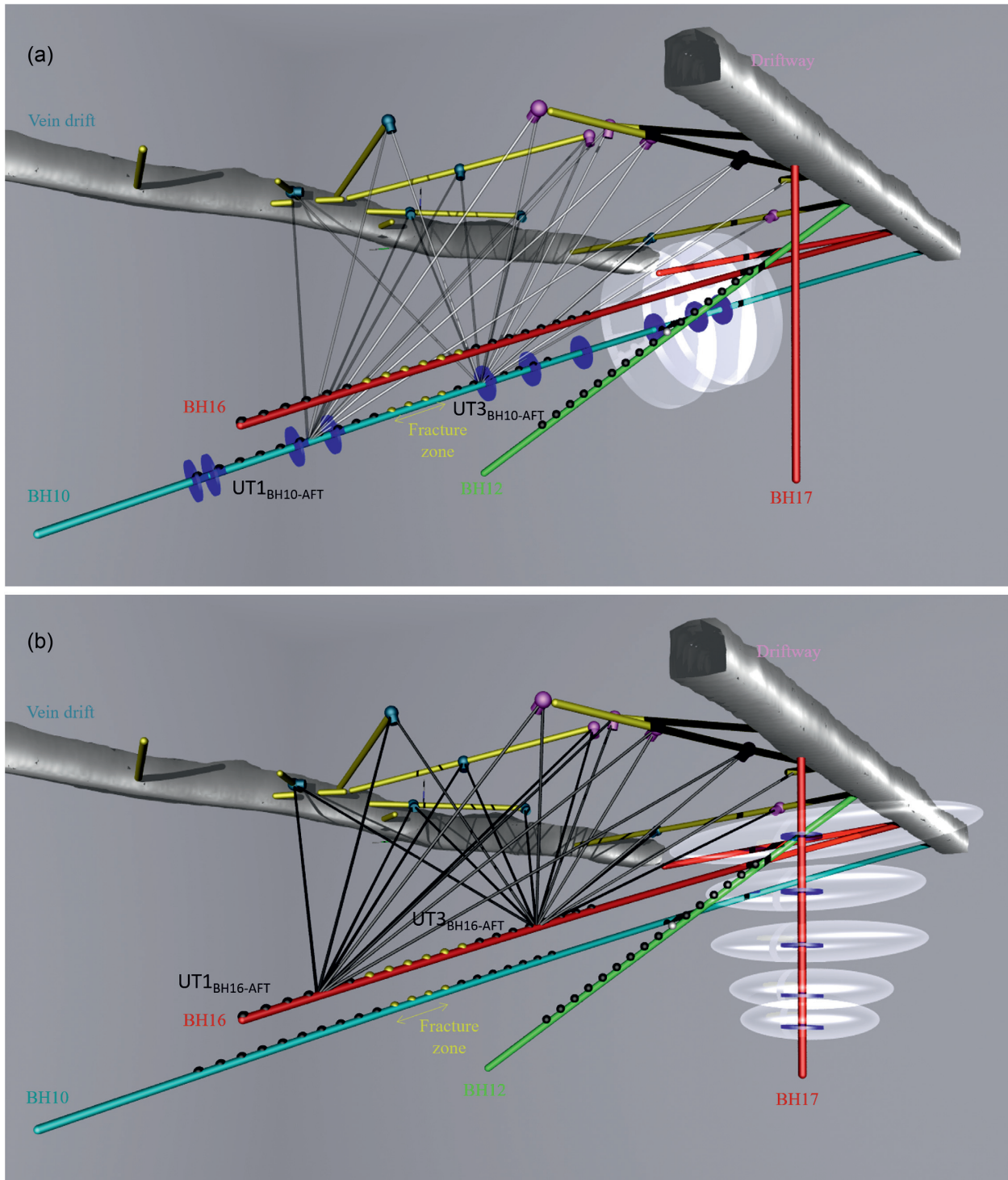
Figure 3. Visualization of UT groups (a) UT1$_{BH10-AFT}$, UT3$_{BH10-AFT}$ and (b) UT1$_{BH16-AFT}$, UT3$_{BH16-AFT}$ in the subparallel boreholes BH10 (light blue) and BH16 (red) with approximated average ray paths (grey and black lines) to the AE sensors. UT groups are marked with black dots. The yellow dots highlight damage zones identified from televiewer logs. The blue circles around borehole BH10 and vertical borehole BH17 show central points of intervals stimulated during the stimulation and validation phases. The white ellipsoids indicate the locations of AE events provoked by the injections.

had to be picked. We selected the noise window at the end of the seismogram (window size of 1024 samples) to avoid distortion during filtering caused by the UT source signal at the beginning of the seismogram. SNR calculation, window overlap and tapering are chosen as in Blanke *et al.* (2019). The seismograms were filtered in

octave-width frequency bands with centre frequencies ranging from 1.5 to 40 kHz.

The Power Spectral Density (PSD) for the pre-defined moving windows and each centre frequency was finally estimated for the selected coda length and noise signal (e.g. Aki & Chouet 1975;

Table 1. Overview of UT group naming in selected boreholes with time and depth interval for which $\overline{Q_C}$ values were estimated.

UT groups	Borehole	Time of UT measurement	Depth interval along borehole (m)[a]	Altitude (m)[b]
UT1$_{BH10-BEF}$	BH10	1 month before stimulation phase in BH10	47–56	270–269
UT3$_{BH10-BEF}$	BH10	1 month before stimulation phase in BH10	36–42	273–272
UT1$_{BH10-AFT}$	BH10	1–2 d after stimulation phase in BH10	47–56	270–269
UT3$_{BH10-AFT}$	BH10	1–2 d after stimulation phase in BH10	36–42	273–272
UT1$_{BH16-AFT}$	BH16	1 d after validation phase in BH17	41–46	271–270
UT3$_{BH16-AFT}$	BH16	1 d after validation phase in BH17	25–33	276–274
UT16$_{BH12-AFT}$	BH12	2 months after validation phase in BH17	7.4–12.4	279–276
UT10$_{BH12-AFT}$	BH12	2 months after validation phase in BH17	14.4–22.4	275–270

[a] Depth intervals are individually measured along each borehole from the well-head. [b] Note altitude is measured positive upwards with respect to normal sea level.

Phillips 1985; Phillips *et al.* 1988):

$$P\ (f, t) =\ C\ (f)\,t^{-m}\exp\left(\frac{-2\pi f t}{Q_C\,(f)}\right), \tag{1}$$

with $C(f)$ as the coda source factor that is assumed to be constant for short distances, t the lapse time and $m = 2$ as the geometrical spreading of body wave amplitudes with time. The exponent is the attenuation term describing the frequency-dependent *S*-coda wave decay with time.

4.2 Regression analysis

The decay of coda amplitudes with time is measured from the temporal decay of spectral amplitudes in the frequency domain:

$$\ln\left(\frac{P(f, t)}{K(\alpha)}\right) =\ \ln\left(C\,(f)\right) - \left(\frac{2\pi f}{Q_C\,(f)}\right)t. \tag{2}$$

Here, t^{-m} was exchanged with $K(\alpha)$ that allows the separation of source and receiver location and contains the geometrical spreading factor α (Sato 1977)

$$K\ (\alpha) =\ \frac{1}{\alpha}\ln\left(\frac{\alpha + 1}{\alpha - 1}\right), \tag{3}$$

with

$$\alpha =\ \frac{t}{t_s}, \tag{4}$$

where t_s is the *S* wave onset time. By using equation (2), the early coda following the direct *S* wave can be analysed (e.g. Gibowicz & Kijko 1994).

For each frequency band, Q_C is estimated from the slope (s) of eq. (2) using linear regression, where the independent and dependent variables are lapse time and coda amplitudes, respectively:

$$Q_C\ (f) =\ \frac{2\pi f}{s}. \tag{5}$$

As part of the regression analysis, the uncertainties σ_{Qc} (2σ standard deviation) are calculated for each $Q_C(f)$ estimate from the slope coefficient estimate. Large σ_{Qc} uncertainties indicate an unstable regressive relation, which typically originated from low SNR conditions, and thus Q_C estimates with $\sigma_{Qc} > 60$ were removed. This reduces the reliable frequency range and we obtain stable Q_C estimates for centre frequencies ranging 3–21 kHz.

4.3 Average Q_C for defined groups of UT measurements

The 3-D setting in the mine complicates the evaluation of Q_C estimates from a single UT recording. Based on information from

the borehole televiewer logs and AE event locations during injection phases, we formed groups of UT measurements from different depth intervals in each of the two boreholes BH10 and BH16 (*cf.* Figs 3 and S2, Supporting Information) to investigate attenuation throughout the mine, and to characterize local damage zones. Each UT group comprises neighbouring UT measurements within a few metres distance of each other. We kept the maximum distance between UT measurements inside a group approximately constant for all defined UT groups. Temporarily separated UT measurements in BH10 before and after the stimulation phase allow us to analyse these two time intervals separately. To better clarify the naming of selected UT groups in different boreholes and from distinct time periods (BEF = before stimulation; AFT = after stimulation), we summarize the labelling of UT groups with a short description of depth and time intervals in Table 1.

The first UT groups (UT1$_{BH10-BEF}$, UT1$_{BH10-AFT}$ and UT1$_{BH16-AFT}$) consist of UT measurements in the deepest parts of the respective boreholes below the damage zone identified in the borehole televiewer logs (*cf.* Figs 1b, 3 and S2, Supporting Information). The second UT groups (UT3$_{BH10-BEF}$, UT3$_{BH10-AFT}$ and UT3$_{BH16}$) consist of UT measurements directly above this damage zone. The separation of groups UT1 and UT3 facilitates to compare Q_C estimates from both sides of the damage zone. This helps evaluating the extent of the damage zone and its impact on wave attenuation. For each UT group, we estimated mean Q_C ($\overline{Q_C}$) curves to each AE sensor (see also Blanke & Boese 2022) to further stabilize the observations. Mean Q_C estimates are built from a minimum number of three UT recordings using the arithmetic mean. However, for group UT1$_{BH16-AFT}$ often only 1–2 UT measurements were available due to the short length of the borehole beyond the damage zone. Thus, the respective $\overline{Q_C}$ curves might be less stable compared to the other curves.

We also define two UT groups using UT measurements in borehole BH12 that are taken from depth intervals corresponding to crossover depths with boreholes BH16 (UT16$_{BH12-AFT}$) and BH10 (UT10$_{BH12-AFT}$) only a few metres (∼4–8 m) below (see also Fig. S2b, Supporting Information). UT measurements in BH12 were made two months after the injections in borehole BH17 during the validation phase. Data of BH12 were analysed because of their comparability in space with UT3 groups of BH10 and BH16, and to facilitate detection of temporal or permanent attenuation changes in this area after hydraulic stimulation phases.

5 RESULTS

In the following, we analyse the spatiotemporal variations of attenuation in the STIMTEC rock volume using UT groups of boreholes

BH10, BH12 and BH16. By splitting the results into observations made at AE sensors along the driftway and vein drift, spatial attenuation changes in the rock volume become apparent. The inspection of temporally divided $\overline{Q_C}$ estimates of UT groups with regard to hydraulic stimulation phases provides information on temporal or semipermanent modification of the local fracture network around the injection intervals.

5.1 Spatiotemporal Q_C observations

Fig. 4 displays $\overline{Q_C}$ curves obtained for each AE sensor using all analysed UT groups from the subparallel boreholes BH10 and BH16 (*cf*. Table 1). The results are separately displayed as $\overline{Q_C}$ curves obtained for sensors along the driftway in Fig. 4(a) (AE02, AE07, AE08, AE09, AE10) and sensors along the vein drift in Fig. 4(b) (AE01, AE03, AE05, AE04, AE12). Ray paths of UT measurements at different depths in the boreholes are partially dissimilar, which provides information on changes in attenuation characteristics in various directions. By comparing the deeper borehole measurements of both boreholes (UT1 groups, dashed lines) with the shallower measurements (UT3 groups, solid lines), it is generally seen that $\overline{Q_C}$ estimates of UT1 groups show on average higher Q_C values. Especially at sensors AE06, AE08 and AE12, higher $\overline{Q_C}$ estimates up to high centre frequencies >15 kHz (longer $\overline{Q_C}$ curves) are obtained for the UT1 groups. At sensors located in the central area of the rock volume (AE10, AE07, AE09, AE04), $\overline{Q_C}$ curves are much shorter and towards the south (AE01, AE02, AE03) no $\overline{Q_C}$ estimates could be obtained for UT1 groups. We see a trend that $\overline{Q_C}$ curves obtained for driftway sensors are on average shorter (more damped) than for vein drift sensors.

The shallower UT3 groups of both boreholes (solid lines) generally provide longer $\overline{Q_C}$ curves, indicating that high frequencies (>15 kHz) are not as much damped as for the deep UT1 groups (dashed lines). However, the $\overline{Q_C}$ values of UT3 are on average lower compared to UT1 groups. The reference line at $Q_C = 140$ highlights that Q_C values along the driftway are lower compared to Q_C values along the vein drift. Estimates obtained at sensors AE09 and AE10 show generally the lowest values. Note that estimates from BH16 (solid black line) are always lower than estimates from BH10 (grey and red lines). The largest difference in $\overline{Q_C}$ estimates between boreholes BH10 and BH16 can be observed at sensors AE01-03. Ray paths to these three sensors are oriented differently than ray paths to the other sensors and they cross the area in which the largest number of AE events occurred during the stimulation phase (cf. Figs 3a and b; fig. 5 of Boese *et al.* 2022). By comparing $\overline{Q_C}$ curves of UT3 groups of BH10, little to no changes in $\overline{Q_C}$ values are recognizable for UT ray paths to sensors that do not cross the stimulated rock volume as marked by AE events. At these sensors, the difference of $\overline{Q_C}$ values is lower between BH10 and BH16 and thus between injection phases.

5.1.1 Influence of hydraulic stimulation phases on Q_C estimates

The systematic temporal decrease of $\overline{Q_C}$ values of the shallow UT3 measurements described above can be clearly related to hydraulic stimulation. The UT3 group in BH10 before the stimulation phase in 2018 (red solid lines) mainly exhibits significantly larger Q_C estimates compared to UT3 measurements in BH16 after the validation phase in 2019 (black solid lines). In the following, we selected only

$\overline{Q_C}$ curves of UT groups in BH10 and BH16 after each stimulation phase and compare these with the nearby UT groups of BH12 (measurements from 2 months after the injection). We illustrate in Fig. 5 that the decrease of $\overline{Q_C}$ values is persistent with time and that relaxation time likely initiates healing of the fracture network in the monitored rock volume. About 13 months passed between the UT measurements in BH10 (grey lines) and BH16 (black lines), 2 months between BH16 and BH12 (dark green lines) and 15 months between BH10 and BH12 (light green lines).

At the driftway sensors $\overline{Q_C}$ estimates at low frequencies (<15 kHz) are within the error bounds and mostly overlap for all time periods indicating no significant change in attenuation and the fracture network after injections stopped. At higher frequencies (>15 kHz), both UT groups in BH12 are more similar to BH10 estimates and thus show a slight rise in $\overline{Q_C}$ values with time. At all vein drift sensors (Fig. 5b), except for sensor AE01, we observe similar characteristics with respect to the error bars. However, compared to the shallow UT3$_{BH16-AFT}$ group in BH16 (black line), the nearby located UT16$_{BH12-AFT}$ group in BH12 (dark green line) does not provide $\overline{Q_C}$ estimates at high frequencies (>15 kHz) along the vein drift sensors, which is indicated by much shorter curves at comparable sensor distances.

The lowest $\overline{Q_C}$ values are obtained at sensors AE01-02 and AE09-10 indicated by the horizontal reference line. Ray paths towards these sensors pass directly through areas where hydraulic injections induced most of the AE events (*cf*. Fig. 3).

### 5.1.2 Azimuthal and distance dependence of Q_C

The differences in $\overline{Q_C}$ estimates between the vein drift and driftway sensors, the shallow and deep UT groups and before and after hydraulic stimulation phases show that attenuation varies in space and time. Despite the temporal variations in Q_C estimates, specific areas in the URL exhibit always larger or lower attenuation characteristics. To better identify these, we plotted $\overline{Q_C}$ estimates of selected centre frequencies with distance (Fig. 6) and with azimuthal angle (Fig. 7) from the centre of each UT group. High-frequency measurements are missing for UT1 groups in both boreholes especially for the more distant sensors, as already shown in Fig. 4. This indicates that distances to the AE sensors become too large to reliably capture the high frequencies of the UT coda waves. Thus, the evaluation of variations of $\overline{Q_C}$ estimates is limited for these deeper measurements and we show respective figures for UT1 groups in Figs S3, S4, S5 and S6 (Supporting Information).

Distance plots of UT3 groups (Fig. 6) in boreholes BH10 and BH16 illustrate that $\overline{Q_C}$ values do not depend on distance in general. We show that frequencies > 15 kHz are recorded to distances of up to 25 m from the UT groups. However, $\overline{Q_C}$ estimates seem to increase at specific sensors (AE12 and AE04) and are often lower at sensors AE08-10. Looking at the azimuthal plots (Fig. 7), a clear trend of larger $\overline{Q_C}$ estimates specifically at high centre frequencies (>15 kHz) becomes obvious at vein drift sensors for azimuths between 60° and 180°. When comparing the estimates in both boreholes at 20 kHz (star markers), BH10 indicates a significant change in $\overline{Q_C}$ throughout the mine from $\overline{Q_C} = 230-130$ (approx. 44 per cent variation of Q_C throughout the mine) and BH16 from $\overline{Q_C} = 181-104$ (approx. 43 per cent variation), whereas at low frequencies $\overline{Q_C}$ is more stable between driftway and vein drift. Similar observations are made for BH12 (Figs S7 and S8, Supporting Information).
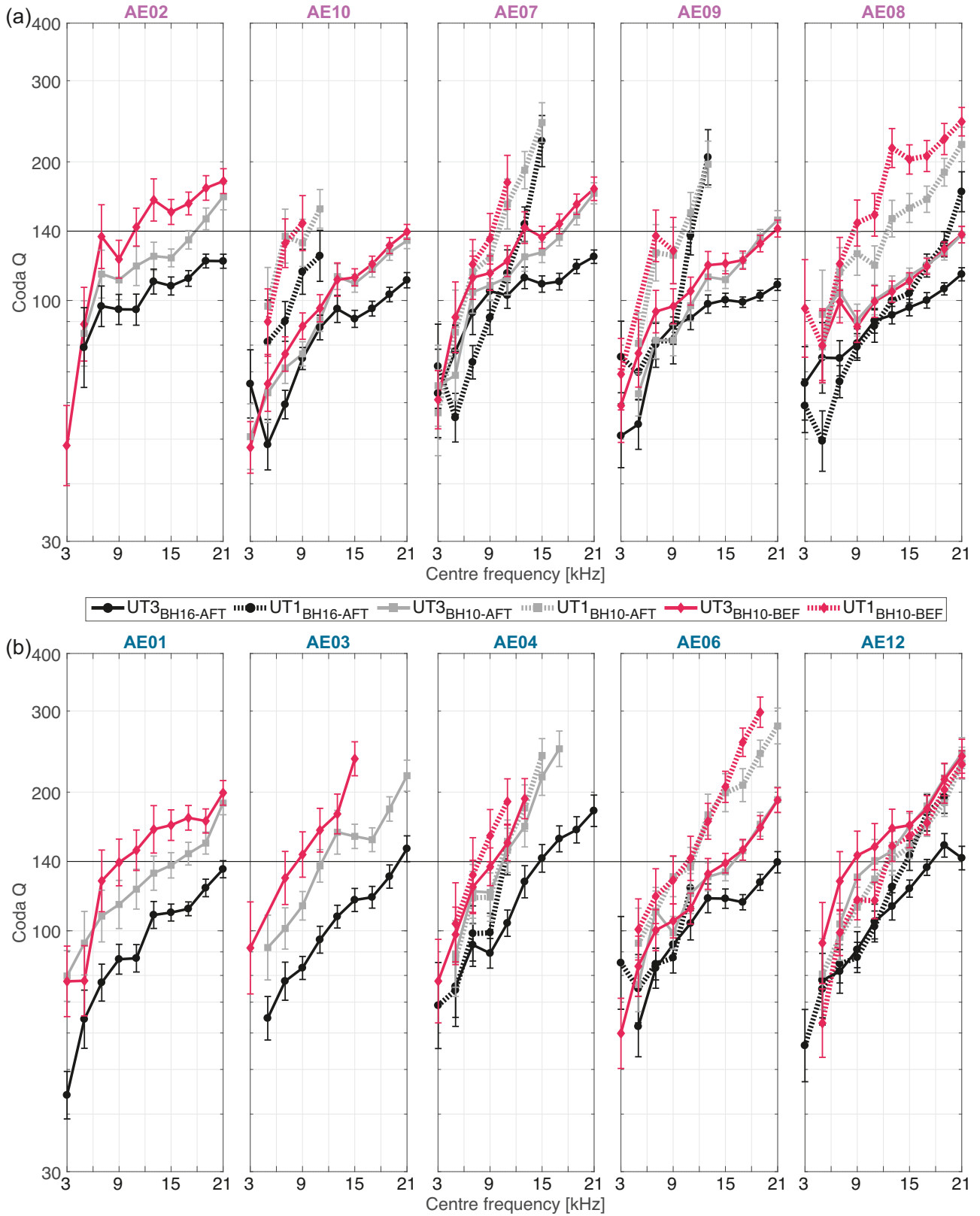
Figure 4. $\overline{Q_C}$ curves estimated for groups of UT measurements in boreholes BH10 (UT1$_{BH10\text{-}BEF}$, UT1$_{BH10\text{-}AFT}$, UT3$_{BH10\text{-}BEF}$, UT3$_{BH10\text{-}AFT}$) and BH16 (UT1$_{BH16\text{-}AFT}$, UT3$_{BH16\text{-}AFT}$) for sensors along (a) the driftway and (b) the vein drift. The colours indicate BH10 before stimulation phase (red), BH10 after stimulation phase (grey) and BH16 after validation phase (black). Line types represent analysed deep UT1 groups (dotted) and shallow UT3 groups (solid). For visual reasons, error bars indicate the 1σ standard deviation. The horizontal line at $Q_C = 140$ serves as a reference line to better highlight differences in estimates at both gallery sites.
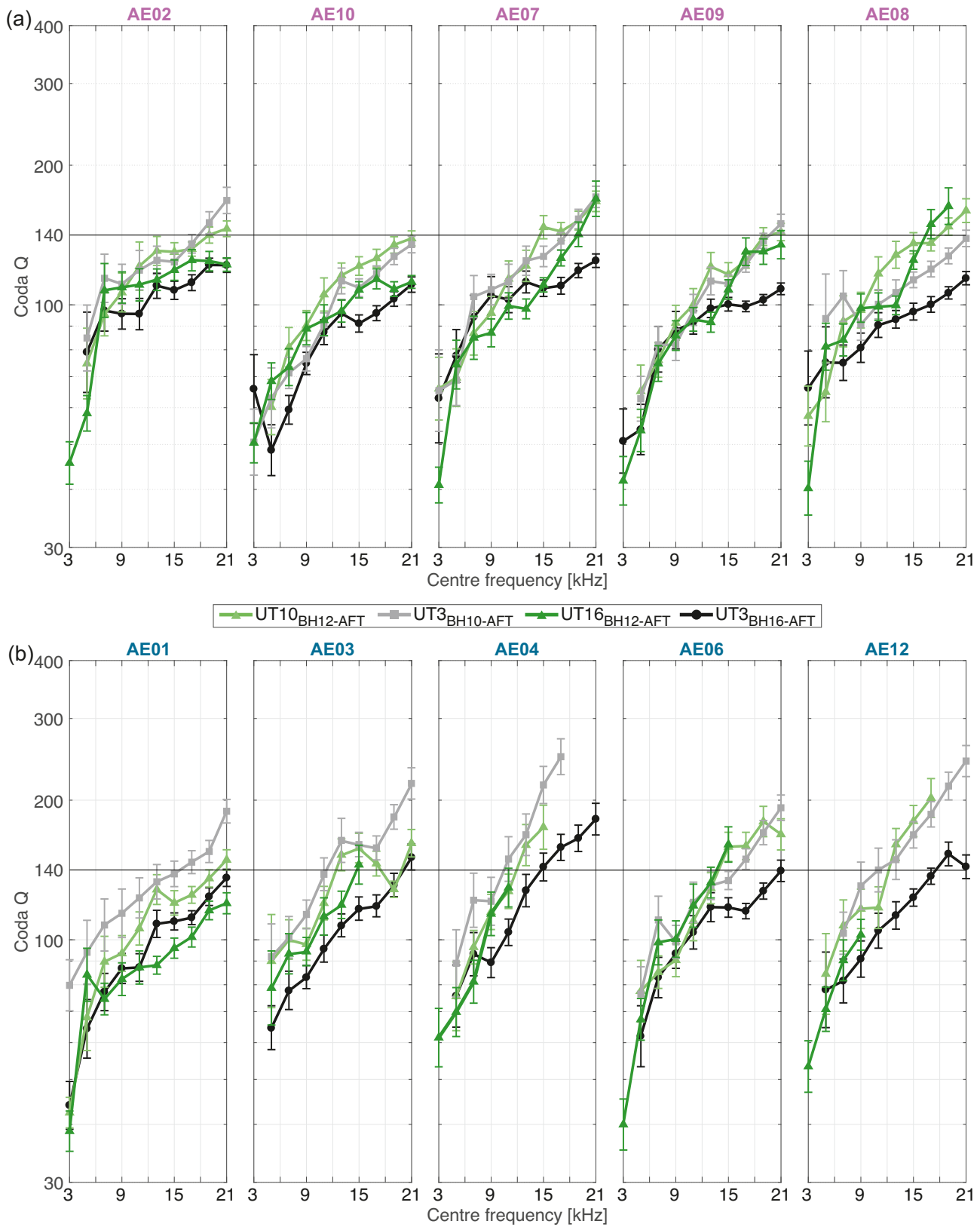
Figure 5. Sensors along the driftway (a) and vein drift (b) showing $\overline{Q_C}$ curves estimated from groups of UT measurements in boreholes BH10 (UT3$_{\text{BH10-AFT}}$), BH16 (UT3$_{\text{BH16-AFT}}$) and BH12 (UT10$_{\text{BH12-AFT}}$, UT16$_{\text{BH12-AFT}}$) after injection phases. For visual reasons, error bars indicate the 1σ standard deviation. The horizontal line at $Q_C = 140$ serves as a reference line to better highlight differences in estimates at both gallery sites.
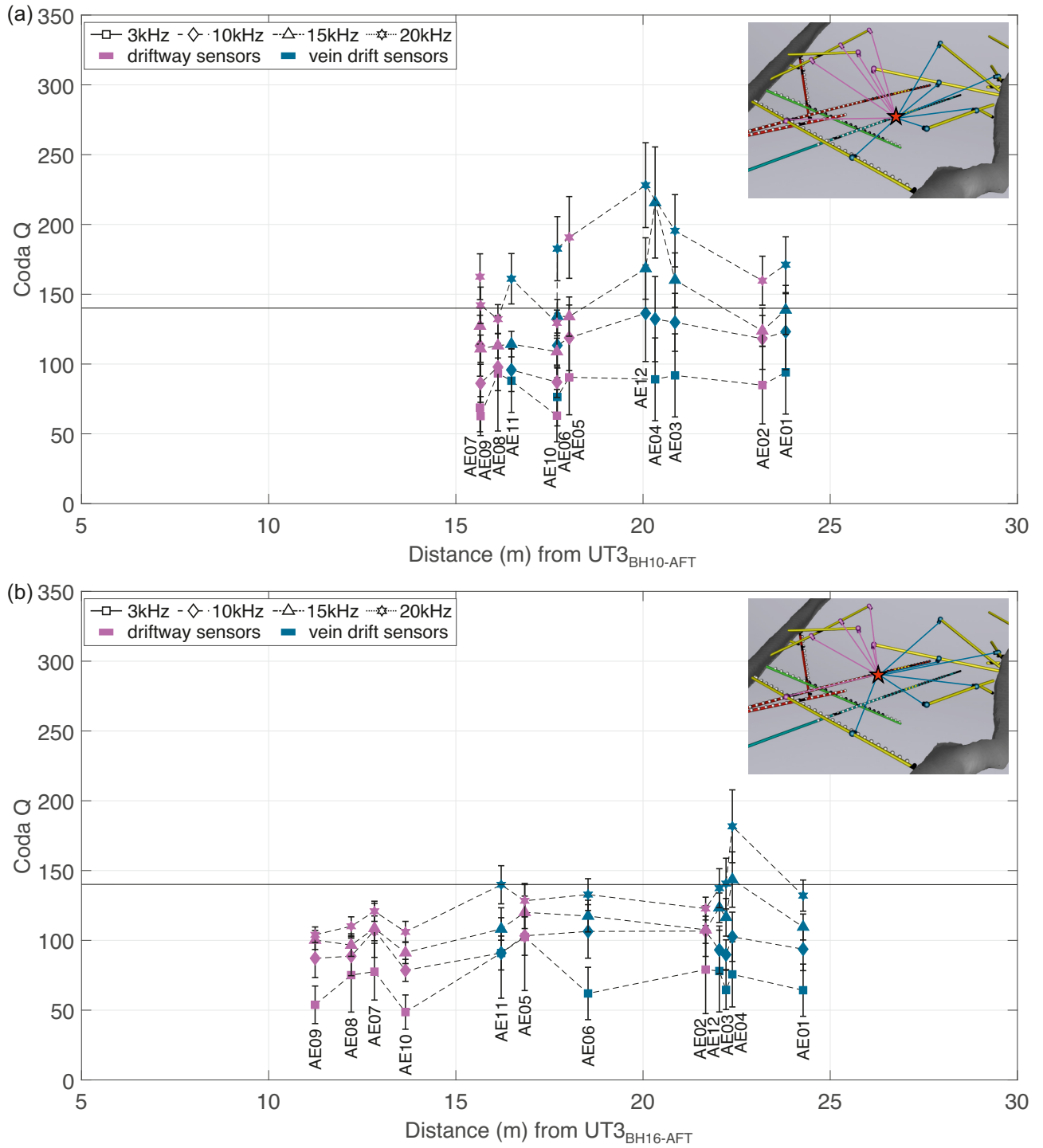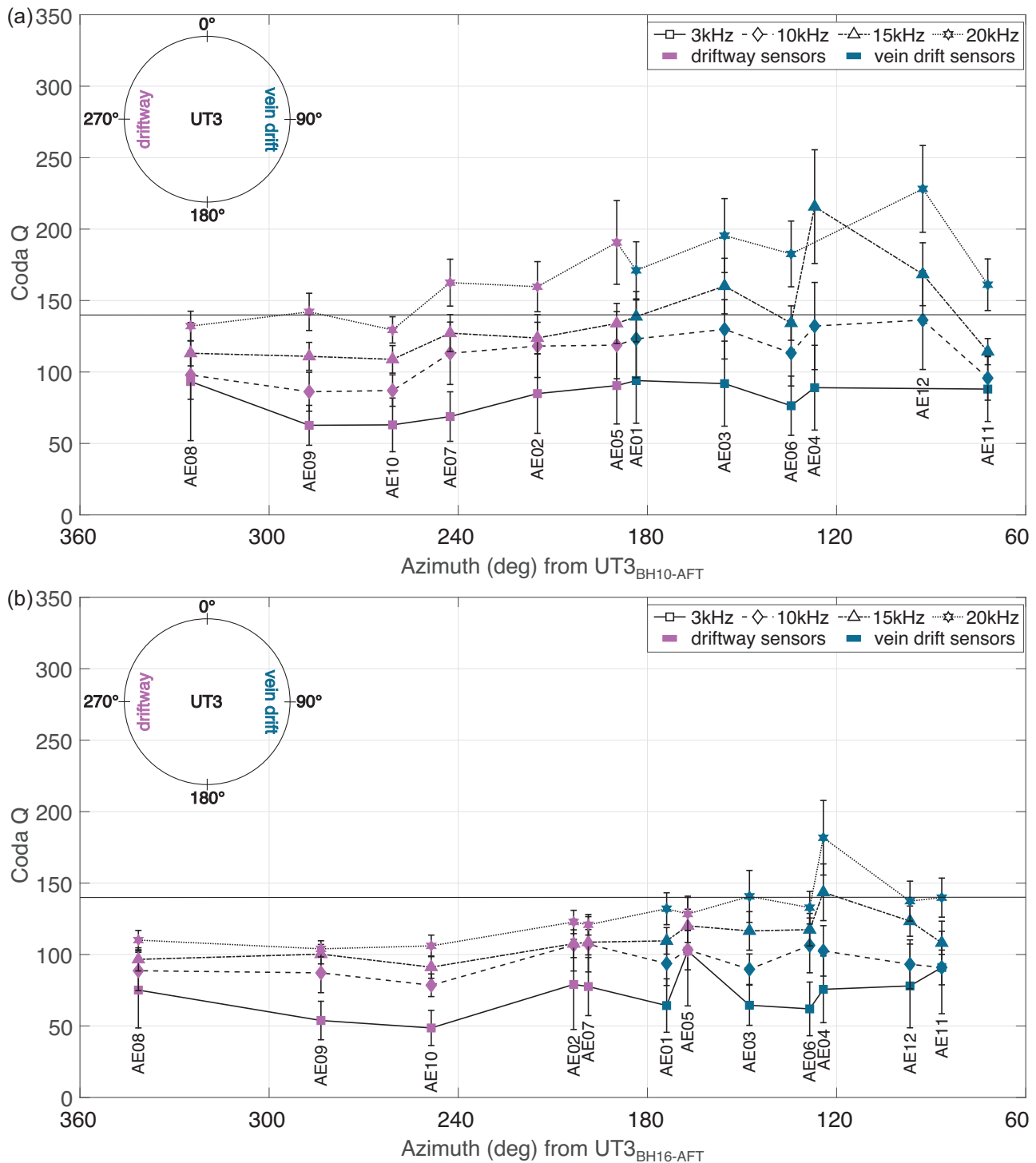
Figure 6. $\overline{Q_C}$ estimates from selected centre frequencies of octave-width frequency bands plotted with distance from centre of UT groups (a) UT3$_{BH10\text{-}AFT}$ and (b) UT3$_{BH16\text{-}AFT}$ to AE sensors. The symbols present selected centre frequencies (3, 10, 15 and 20 kHz). The colours indicate sensors along the driftway (magenta) and vein drift (turquoise). Error bars indicate the 2σ standard deviation (σ_{Qc}). The inset shows 3-D perspective view with centre of UT group (star marker) and average seismic ray path to sensors along the driftway (magenta lines) and vein drift (turquoise lines). The horizontal line at $Q_C = 140$ serves as a reference line across all plots.

6 DISCUSSION

Our study shows that the analysis of UT coda wave amplitudes is a powerful tool in analysing reservoir rock damage and spatiotemporal changes related to stimulation campaigns. UT coda wave analysis was previously not much used at the URL and laboratory scale. Based on the single isotropic scattering model, we used the early S-coda waves of active UT measurements to estimate the frequency-dependent coda quality factor Q_C at twelve AE

Figure 7. $\overline{Q_C}$ estimates from selected centre frequencies of octave-width frequency bands estimated at each AE sensor and plotted against azimuthal distance from groups (a) UT3$_{BH10-AFT}$ and (b) UT3$_{BH16-AFT}$. The colours indicate sensors along the driftway (magenta) and vein drift (turquoise). The symbols present selected centre frequencies (3, 10, 15 and 20 kHz). Error bars indicate the 2σ standard deviation (σ_{Qc}). The horizontal line at $Q_C = 140$ serves as a reference line across all plots.

sensors in anisotropic metamorphic gneiss at the URL-RZ. The high-frequency (1–60 kHz) UT measurements have wavelengths in the range of length scales of faults and joints (approx. 0.16–1.6 m). Both are assumed to strongly interact with each other and thus scattering effects are expected to contribute significantly to attenuation processes influencing the recorded signals. Elastic anisotropy and

changing characteristics of the studied rock volume may affect scattering processes in varying directions leading to dissimilar observations of UT waveforms at different AE sensors. Finally, hydraulic stimulation of existing fracture networks may also locally affect scattering attenuation temporarily and/or semipermanently (thereby providing the base for imaging stimulation-induced changes in the

target reservoir). In addition to that, the complex set-up of differently oriented boreholes, various UT measurement campaigns and several hydraulic stimulation phases within the STIMTEC project render analysis of scattering attenuation in the URL difficult. Thus, we focused on a number of selected boreholes (BH10, BH12, BH16) and specific UT groups consisting of 88 spatially selected UT measurements above and below a suspected damage zone detected by borehole televiewer logs (e.g. Fig. 1b), and before and after hydraulic injections. This allowed us to successfully monitor local structural changes by comparing $\overline{Q_C}$ estimates in space and time.

6.1 Spatial variation of Q_C estimates

We obtained stable Q_C estimates for centre frequencies between 3 and 21 kHz. Similar to field scale studies, we found Q_C to increase with frequency (e.g. Novelo-Casanova & Lee 1991; Plenkers *et al.* 2009; Calvet & Margerin 2013; Blanke *et al.* 2019). To compare the frequency dependence with other studies, we fitted $\overline{Q_C}$ curves to the parametric model (Fig. S9, Supporting Information)

$$Q_C(f) = Q_0 \, f^n \tag{6}$$

that describes the frequency dependence of coda Q with Q_0 being the quality factor Q_C at the reference frequency $f = 1$ Hz (e.g. Morozov *et al.* 2008; Sato *et al.* 2012). The calculated exponent n ranges between 0.52 and 0.58, which is within the typically observed span of 0.5–1.0 (e.g. Sato, Fehler & Wu 2002; Sato *et al.* 2012). This finding is in part in contrast to observations made in laboratory rock deformation experiments (e.g. Guo *et al.* 2009; Hu *et al.* 2017) in which Q_C is not persistently increasing with frequency. Laboratory UT wavelengths strongly interact with grains in the rock specimen (e.g. Blanke *et al.* 2021), whereas UT wavelengths at the URL and field scale are much larger and remain uninfluenced by grains and grain boundary effects likely leading to different observations for the different seismic scales.

The shallow UT3 groups of the subparallel boreholes BH10 and BH16, as well as the neighbouring UT groups in the perpendicular borehole BH12, indicate large $\overline{Q_C}$ values towards the vein drift and low values along the driftway (e.g. Figs 7 and S7, Supporting Information). This may indicate that the excavation damage zone of the driftway is more pronounced compared to the vein drift. The latter was also suggested by Krauß *et al.* (2014) for lower frequencies in the same rock volume 180 m north of the STIMTEC site showing lower Q_P estimates (≤ 10) along the driftway than along the vein drift ($Q_P \geq 15$, *cf.* their fig. 7b). Slightly larger uncertainties at higher frequencies and for larger $\overline{Q_C}$ estimates (Figs 6, 7, S3 and S8, Supporting Information) are likely related to the incidence angle of the recorded UT waves at sensors close to the galleries and partially due to larger signal-to-receiver distances which may marginally bias the recorded UT coda signals.

Compared to the shallow UT3 groups, higher $\overline{Q_C}$ estimates are obtained using the deeper UT1 groups, however, high-frequency estimates (>15 kHz) are missing at the driftway sensors. Higher $\overline{Q_C}$ values suggest better rock quality in the vicinity of the deep UT1 groups. The abrupt absence of high frequency estimates, however, indicates a damage zone between UT1 groups and the driftway sensors. The cause of strongly damped high-frequency signals could be the same damage zone as that observed in boreholes BH10 and BH16 detected with televiewer logs (Fig. 1b) which is further supported by existing structural markers along the galleries (Fig. 1a). The angle of ray paths (more vertical compared to UT3 group ray paths) towards the driftway sensors might inhibit high-frequencies

to pass through the damage zone. Indications from structural markers and televiewer logs suggest that the damage zone encountered in boreholes BH10 and BH16 crosses the mine in NW-SE direction affecting mostly sensor AE09 (Fig. S10, Supporting Information). The damage zone thickness and the vertical dimension remain unknown but the larger $\overline{Q_C}$ estimates at sensors north of the damage zone (e.g. AE08, AE11, AE12, AE06) and a sudden absence of high-frequency Q_C estimates at sensors along the driftway (AE09, AE10) which are, however, closely located to UT1 groups, support the assumption of a fault structure that extends between the galleries.

By contrast to UT1 groups, $\overline{Q_C}$ estimates of the shallower UT3 groups do not provide clear evidence of the existence of an NE–SW trending damage zone. We observe high $\overline{Q_C}$ estimates at sensors AE12 and AE04 to which seismic rays need to travel through the expected damage zone. Also, the observations from BH12 show higher $\overline{Q_C}$ estimates for sensor AE11 and partially for sensors AE05 and AE12. It could be that the damage zone varies in thickness and may not extend completely upwards to the AE sensors. UT3 groups in BH10 and BH16 and UT groups in BH12 are several metres above UT1 groups which could cause seismic rays from shallower depths and also with opposite ray paths to circumvent or only slightly pass through the damage zone. However, we assume that the overall low $\overline{Q_C}$ values observed at sensors AE09 and AE10 might be biased by their position within the excavation damage zone and the location close to the driftway tunnel, the assumed damage zone close to sensor AE09 and the ray paths of UT groups through stimulated rock volume.

6.2 Q_C variation due to hydraulic stimulation

Hydraulic stimulation produced new fractures and activated the existing fracture network surrounding the boreholes. Fig. 4 shows a clear drop of $\overline{Q_C}$ values after the first stimulation in BH10 (UT3$_{BH10\text{-}BEF}$ versus UT3$_{BH10\text{-}AFT}$) and even lower $\overline{Q_C}$ values after the second stimulation in BH17 (UT3$_{BH16\text{-}AFT}$) at sensors close to the zones where AE events occurred (Fig. S10, Supporting Information). The maximum estimated $\overline{Q_C}$ values at around 20 kHz dropped here about 21–23 per cent on average between the two stimulation phases. This indicates enhanced rock damage and an activation of the local fracture network due to fluid injection. By contrast, $\overline{Q_C}$ curves for ray paths along injection points that showed no AE activity (e.g. in the deepest borehole section of BH10) remain stable before and after stimulation periods indicating no significant change of the local fracture network. Borehole BH16 systematically shows the lowest $\overline{Q_C}$ estimates at all sensors (Fig. 4). This could be explained by the influence of increased damage close to BH16, caused by the hydraulic stimulations in BH10 and the vertical borehole BH17 that also produced AE events indicating an additional change in the local fracture network around it. $\overline{Q_C}$ estimates of UT groups in BH12 provide evidence that larger injection-induced fractures, which are sampled by lower frequencies, remain after the stimulations. In contrast, smaller induced fractures, sampled by higher frequencies, seem to heal with time. This is indicated by overall overlapping $\overline{Q_C}$ curves in Fig. 5 at centre frequencies <15 kHz but increasing $\overline{Q_C}$ estimates for BH12 at centre frequencies >15 kHz that suggest microfracture healing. However, comparing $\overline{Q_C}$ curves of BH12 and BH10 (grey and light green lines in Fig. 5), clearly shows that the induced fractures do not heal completely after the 13–15 months as $\overline{Q_C}$ curves of BH12 are still below the values from BH10 before any injection took place (red lines in Fig. 4). We
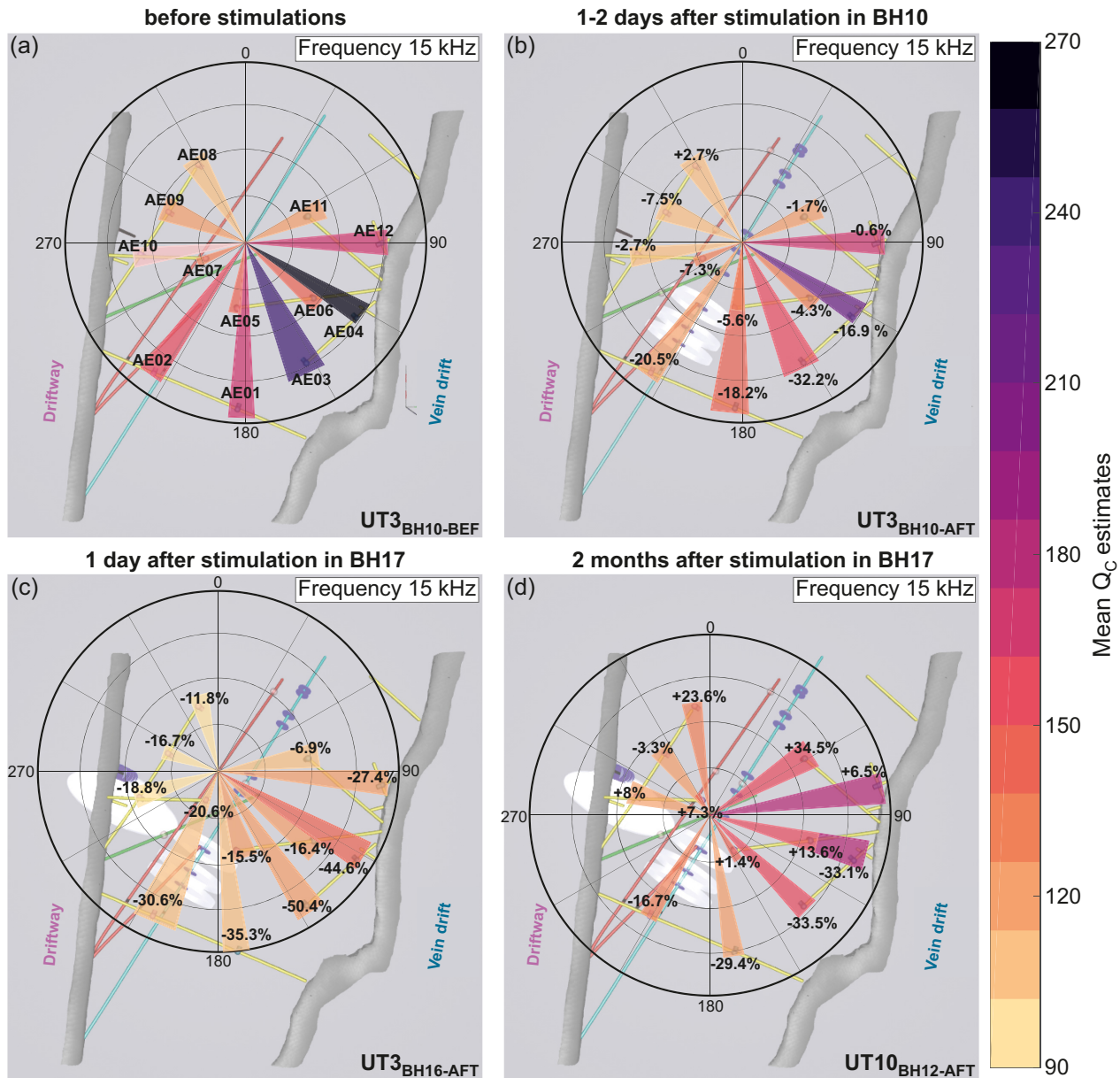
Figure 8. Comparison of $\overline{Q_C}$ changes before and after stimulations for centre frequency 15 kHz. The colour bar shows $\overline{Q_C}$ values. The colour-coded pie chart within the stereonet visualize $\overline{Q_C}$ estimates between respective AE sensors and UT groups (a) before any stimulation (UT3$_{BH10-BEF}$), (b) 1–2 d after the stimulation phase (UT3$_{BH10-AFT}$), (c) 1 d after the validation phase (UT3$_{BH16-AFT}$) and (d) 2 months after the validation phase (UT10$_{BH12-AFT}$). The percentages show the changes in $\overline{Q_C}$ values with time based on the initial $\overline{Q_C}$ values in subfigure 8(a) and are related to the colour-coded pie charts. Negative values indicate reduction of $\overline{Q_C}$, positive values indicate increase of $\overline{Q_C}$.

summarize and visualize the spatial and temporal variations of $\overline{Q_C}$ estimates in the STIMTEC project site in Fig. 8 where we show the spatial distribution of $\overline{Q_C}$ estimates at 15 kHz centre frequency during four stages before and after hydraulic stimulation periods. At each sensor the temporal changes of $\overline{Q_C}$ values are indicated by colour and also by percentages, which are based on the initial $\overline{Q_C}$ estimates in Fig. 8(a).

6.3 *In-situ* lab application of coda-*Q*

At the field scale, coda *Q* can be used to investigate attenuation changes due to, for instance, long-term geothermal energy production, existence of fault zones or large geological features (e.g.

Blanke *et al.* 2019). However, the considered larger wavelengths (λ = approx. 35–3500 m) and lower frequencies (<100 Hz) as well as boundary conditions such as large source-to-receiver distances at this scale prevent us from resolving small-scale structural variations at the mesoscale due to hydraulic stimulation. Experiments in URLs can help us to better understand where and how hydraulic stimulation temporarily or permanently impact the local rock quality in a reservoir. Smaller wavelengths of UT measurements (approx. 0.16–1.6 m) can be used to detect damage and healing of the local fracture network. We show in this study that we are able to assess an upper limit for the time span that is needed for small fractures to heal, or evaluate whether hydraulic injections locally change the rock quality permanently or temporarily. These observations can

be useful in future studies to enhance our understanding of fracture processes important for mining activities, reservoir exploitation and underground storage of gases and liquids.

Field studies (e.g. Hiramatsu *et al.* 2000; Zhu *et al.* 2017) suggest that coda Q analysis might be more sensitive to inhomogeneities in the crust than velocity measurements. Our results also show that coda Q analysis detects small-scale variations in the local fracture network better than velocity measurements (i.e. Q_C is more sensitive to changes). While direct Q measurements in the URL-RZ show a reduction of approx. 10 per cent in the damage zones (e.g. Krauß *et al.* 2014), *P*-wave velocities exhibit only 2–7 per cent reduction at frequencies 100–3000 Hz (e.g. Krauß *et al.* 2014; Boese *et al.* 2022). Coda Q varies up to ∼40–50 per cent throughout the STIMTEC volume (see e.g. Figs 7a and 8) and on average 21–23 per cent in its maximum and minimum values between single stimulations. Thus, we conclude coda analysis of active UT measurements is a valuable tool for georeservoir real-time monitoring for higher frequencies (up to 21 kHz) as compared to e.g. CASSM (Continuous Active-Source Seismic Monitoring; Marchesini *et al.* 2017).

7 CONCLUSION

We investigated scattering attenuation at the mesoscale using *S*-coda waves of spatially selected 88 UT measurements acquired during the STIMTEC project in the URL-RZ in Freiberg, Germany. Using the single scattering approach of Phillips (1985), we obtained stable Q_C estimates for predefined centre frequencies (3–21 kHz) of octave-width frequency bands and show that the frequency dependence of Q_C estimates at the mesoscale is comparable to observations at the field scale. We assumed that UT wavelengths are of similar length scale (0.6–1.6 m) as the small-scale inhomogeneities (fractures and joints) of the investigated rock volume at the URL. This poses an advantage over field-scale studies, which analyse much longer wavelengths, because temporal and permanent changes of the local fracture network induced by small-scale hydraulic stimulations can be detected and monitored.

Up to date, frequency-dependent coda Q analysis has been rarely used in URLs and in studies that deal with high frequencies >1 kHz. We find that coda wave analysis is more robust in validating or detecting major damage zones in the investigated rock volume compared to other methods, such as direct-Q or *P*-wave velocity applications. We observe a significant drop (up to 21–23 per cent) of Q_C estimates after each hydraulic stimulation phase at specific sensors (e.g. towards the vein drift) in accordance with the local occurrence of induced AE events due to the stimulation. High frequency (>15 kHz) Q_C values of UT measurements two months after the injections suggest healing of small-scale induced fractures. Larger fractures by contrast, which can be detected by analysing lower frequencies (<15 kHz), do not seem to heal within the analysed time span. A comparison of spatially separated UT groups at deeper and shallower depths surrounding a damage zone reveal: (1) Scattering attenuation is more dominant towards the driftway which likely indicates a larger extent and/or higher attenuation of the excavation damage zone compared to the vein drift. (2) Variations of Q_C estimates at specific sensors provide an indication of an existing damage zone extending NW–SE between the galleries. The latter is in line with pervious observations from borehole televiewer logs, structural markers along the galleries and seismic velocity survey.

Our analysis shows that coda Q is also a powerful tool to detect temporal or permanent local changes of fracture networks resulting from stimulation. We conclude that coda Q analysis may represent a useful tool for studies in URLs and real-time monitoring of georeservoirs related to, for example, liquid and gas storages or geothermal energy projects complementing other methods such as CASSM.

DATA AVAILABILITY

All active UT transmission data used in this study, sensor coordinates, measurement recording times and positions as well as manually identified phase arrivals are available at the GFZ Data Services via https://doi.org/10.5880/GFZ.4.2.2021.002 (License CC BY 4.0). The catalogues of mean coda Q estimates of selected boreholes, sensor and UT group locations are accessible in table format via the GFZ Data Services (https://doi.org/10.5880/GFZ.4.2.2022.004, License CC BY 4.0).

REFERENCES

Abercrombie, R. E., 1995. Earthquake source scaling relationships from −1 to 5 ML using seismograms recorded at 2.5-km depth, *J. geophys. Res.,* **100,** 24 015–024 036.

Abercrombie, R. E., 1998. A summary of attenuation measurements from borehole recordings of earthquakes: the 10 Hz transition problem, in *Q of the Earth: Global, Regional, and Laboratory Studies, Pageoph Topical Volumes,* eds Mitchell, B. J. & Romanowicz, B., Birkhäuser, doi: 10.1007/978-3-0348-8711-3_11.

Abercrombie, R. E., 2000. Crustal attenuation and site effects at Parkfield, California, *J. geophys. Res.,* **105**(B3), 6277–6286.

Abercrombie, R. E., 2015. Investigating uncertainties in empirical Green's function analysis of earthquake source parameters, *J. geophys. Res.,* **120**(6), 4263–4277.

Abercrombie, R. E., 2021.Resolution and uncertainties in estimates of earthquake stress drop and energy release, Philos. Trans. R. Soc. A., **379**: 20200131, doi: 10.1098/rsta.2020.0131.

Adams, D. A. & Abercrombie, R. E., 1998. Seismic attenuation above 10 Hz in southern California from coda waves recorded in the Cajon Pass borehole, *J. geophys. Res.,* **103**(B10), 24 257–224 270.

Adero, B., 2020. *Experimental investigations of mechanical anisotropy of Freiberg gneiss: implications for hydraulic stimulation, PhD thesis,* Ruhr-Universität Bochum, Germany, doi: 10.13154/294-7755.

Aki, K., 1969. Analysis of the seismic coda of local earthquakes as scattered waves, *J. geophys. Res.,* **74**(2), 615–631.

Aki, K., 1980a. Attenuation of shear-waves in the lithosphere for frequencies from 0.05 to 25 Hz, *Phys. Earth planet. Inter.,* **21**(1), 50–60.

Aki, K., 1980b. Scattering and attenuation of shear waves in the lithosphere, *J. geophys. Res.,* **85**(B11), 6496–6504.

Aki, K., 1981. Attenuation and scattering of short-period seismic waves in the lithosphere, in Husebye, E., Mykkeltveit, S., Husebye, E. & Mykkeltveit, S., *Identification of Seismic Sources – Earthquake or Underground Explosion (NATO Advanced Study Institutes Series),* Vol. 74, pp. 515–541, Springer, doi: 10.1007/978-94-009-8531-5_28.

Aki, K. & Chouet, B., 1975. Origin of coda waves: source, attenuation, and scattering effects, *J. geophys. Res.,* **80**(23), 3322–3342.

Blanke, A. & Boese, C. M., 2022. *Frequency-dependent quality factors of S-coda waves from active ultrasonic transmission measurements in the STIMTEC project, URL Reiche Zeche, Germany,GFZ Data Services,* doi: 10.5880/GFZ.4.2.2022.004.

Blanke, A., Kwiatek, G., Goebel, T. H. W., Bohnhoff, M. & Dresen, G., 2021. Stress drop-magnitude dependence of acoustic emissions during laboratory stick-slip, *Geophys. J. Int.,* **224**(2), 1371–1380.

Blanke, A., Kwiatek, G., Martínez-Garzón, P. & Bohnhoff, M., 2019. Sensitivity and stability analysis of coda quality factors at The Geysers geothermal field, California, *Bull. seism. Soc. Am.,* **109**(3), 959–975.

Boese, C. M., Kwiatek, G., Fischer, T., Plenkers, K., Starke, J., Blümle, F., Janssen, C. & Dresen, G., 2022. Seismic monitoring of the stimtec hydraulic stimulation experiment in anisotropic metamorphic gneiss, *Solid Earth,* **13**(2), 323–346, doi: 10.5194/se-13-323-2022.

Boese, C. M., Kwiatek, G., Fischer, T., Plenkers, K., Starke, J., Blümle, F., Dresen, G. & Janssen, C., 2021. *Ultrasonic transmission measurements from six boreholes from the STIMTEC experiment, Reiche Zeche Mine, Freiberg (Saxony, Germany), GFZ Data Services,* doi: 10.5880/GFZ.4.2.2021.002.

Calvet, M. & Margerin, L., 2013. Lapse-time dependence of coda Q: anisotropic multiple-scattering models and application to the Pyrenees, *Bull. seism. Soc. Am.,* **103**(3), 1993–2010.

Calvet, M., Sylvander, M., Margerin, L. & Villaseñor, A., 2013. Spatial variations of seismic attenuation and heterogeneity in the Pyrenees: coda Q and peak delay time analysis, *Tectonophysics,* **608,** 428–439.

Frankel, A. & Wenneberg, L., 1987. Energy-flux model of seismic coda: separation of scattering and intrinsic attenuation, *Bull. seism. Soc. Am.,* **77**(4), 1223–1251.

Gibowicz, S. & Kijko, A., 1994. *An Introduction to Mining Seismology (International Geophysics),* Vol. 55, Academic Press, doi: 10.1016/c2009-0-02348-4.

Giese, R. & Jaksch, K., 2016. GFZ underground laboratory in the research and education mine "Reiche Zeche" Freiberg, *J. Large-Scale Res. Facilities,* **2,** A68, doi: 10.17815/jlsrf-2-131.

Guo, M.-Q., Fu, L.-Y. & Ba, J., 2009. Comparison of stress-associated coda attenuation and intrinsic attenuation from ultrasonic measurements, *Geophys. J. Int.,* **178**(1), 447–456.

Hiramatsu, Y.,Hayashi, N.,Furumoto, M.& Katao, H.,2000. Temporal changes in coda Q-1 and b value due to the static stress change associated with the 1995 Hyogo-ken Nanbu earthquake ,*J. Geophys. Res. Solid Earth,***105**(3), 6141–6151, doi: 10.1029/1999JB900432.

Holliger, K., 1996. Upper crustal seismic velocity heterogeneity as derived from a variety of *P*-wave sonic logs, *Geophys. J. Int.,* **125**(3), 813–829.

Hu, J., Fu, L. Y., Wei, W. & Zhang, Y., 2017. Stress-associated intrinsic and scattering attenuation from laboratory ultrasonic measurements on shales, *Pure appl. Geophys.,* **175**(3), 929–962.

Ide, S., Beroza, G. C., Prejean, S. G. & Ellsworth, W.L., 2003. Apparent break in earthquake scaling due to path and site effects on deep borehole recordings, *J. geophys. Res.,* **108**(B5), 3349–3352.

Johnston, D. H., Toksöz, M. N. & Timur, A., 1979. Attenuation of seismic waves in dry and saturated rocks: II. Mechanisms, *Geophysics,* **44**(4), 691–711.

Krauß, F., Giese, R., Alexandrakis, C. & Buske, S., 2014. Seismic travel-time and attenuation tomography to characterize the excavation damaged zone and the surrounding rock mass of a newly excavated ramp and chamber, *Int. J. Rock Mech. Min. Sci.,* **70,** 524–532.

Kwiatek, G., Plenkers, K., Dresen, G. & JAGUARS Research Group, 2011.Source parameters of picoseismicity recorded at Mponeng Deep-Gold Mine, South Africa: Implications for scaling relations, *Bull. seism. Soc. Am.,* **101**(6),2592–2608, doi: 10.1785/0120110094.

Leary, P. & Abercrombie, R. E., 1994. Frequency dependent crustal scattering and absorption at 5–160 Hz from coda decay observed at 2.5 km depth, *Geophys. Res. Lett.,* **21**(11), 971–974.

Ma, R. & Ba, J., 2020. Coda and intrinsic attenuations from ultrasonic measurements in tight siltstones, *J. geophys. Res.,* **125**, e2019JB018825, doi: 10.1029/2019JB018825.

Marchesini, P., Ajo-Franklin, J. B. & Daley, T. M. 2017. *In situ* measurement of velocity-stress sensitivity using crosswell continuous active-source seismic monitoring, *Geophysics,* **82**, D319–D326.

Morozov, I. B., Zhang, C., Duenow, J. N., Morozova, E. A. & Smithson, S. B. 2008. Frequency dependence of Coda Q, Part I: numerical modeling and examples from peaceful nuclear explosions, *Bull. seism. Soc. Am.,* **98**(6), 2615–2628.

Mukhopadhyay, S., Sharma, J., Massey, R. & Kayal, J., 2008. Lapse-time dependence of coda Q in the source region of the 1999 Chamoli earthquake, *Bull. seism. Soc. Am.,* **98**(4), 2080–2086.

Novelo-Casanova, D. A. & Lee, W., 1991. Comparison of techniques that use the single scattering model to compute the quality factor Q from coda waves, *Pure appl. Geophys.,* **135**(1), 77–89.

Obermann, A., Kraft, T., Larose, E. & Wiemer, S., 2015. Potential of ambient seismic noise techniques to monitor the St. Gallen geothermal site (Switzerland), *J. geophys. Res.,* **120**, 4301–4316.

Phillips, W. S., 1985. *The separation of source, path and site effects on high frequency seismic waves: An analysis using coda wave techniques, PhD thesis,* Massachusetts Institute of Technology, Cambridge, Massachusetts.

Phillips, W. S. & Aki, K., 1986. Site amplification of coda waves from local earthquakes in central California, *Bull. seism. Soc. Am.,* **76**(3), 627–648.

Phillips, W. S., Lee, W. & Newberry, J. T., 1988. Spatial variation of crustal coda Q in California, in *Scattering and Attenuations of Seismic Waves, Part I Pageoph Topical Volumes,* pp. 251–260, eds. Aki, K. & Wu, R.S., Birkhäuser.

Plenkers, K., Kwiatek, G. & Naoi, M., JAGUARS Working Group, 2009. JAGUARS project: attenuation, scattering and instrumental effects of events recorded by a high-frequency seismic network as seen from seismograms and their frequency content, in *Proceedings of the IASPEI General Assembly,* IASPEI, Cape Town, Republic of South Africa, 10–16 January 2009.

Rautian, T. & Khalturin, V., 1978. The use of the coda for determination of the earth- quake source spectrum, *Bull. seism. Soc. Am.,* **68**(4), 923–948.

Renner, J. STIMTEC-Team, 2021. STIMTEC – A mine-scale hydraulic stimulation experiment of anisotropic metamorphic rock with evaluation by mine-back drilling, in *ARMA Newsletter Winter 2021: Introduction to the Special Issue: Deep Underground Laboratories (DUL),* pp. 2–4, ed. Ma, X., ARMA Publications Committee. Available at: https://www.armarocks.org/wp-content/uploads/2021/01/2021_issue_30_winter.pdf (last access: 2022 January).

Sato, H., 1977. Energy propagation including scattering effects single isotropic scattering approximation, *J. Phys. Earth,* **25**(1), 27–41.

Sato, H., Fehler, M. C. & Maeda, T., 2012. *Seismic Wave Propagation and Scattering in the Heterogeneous Earth,* 2nd edn, Vol. 496, Springer, doi: 10.1007/978-3-642-23029-5.

Sato, H., Fehler, M. C. & Wu, R. S., 2002. Chapter 13: Scattering and attenuation of seismic waves in the lithosphere, in *International Handbook of Earthquake and Engineering Seismology,* Vol., **81A,** pp. 195–208, eds, Jennings, P., Kanamori, H. & Lee, W, Academic Press.

Shearer, P. M., Abercrombie, R. E., Trugman, D. T. & Wang, W., 2019. Comparing EGF methods for estimating corner frequency and stress drop from *P* wave spectra, *J. geophys. Res.,* **124**(4), 3966–3986.

Wang, W. & Shearer, P.M., 2018. An improved method to determine coda-Q, earthquake magnitude, and site amplification: theory and application to Southern California, *J. geophys. Res.,* **124,** 578–598.

Wei, W. & Fu, L.-Y., 2014. Monte Carlo simulation of stress-associated scattering attenuation from laboratory ultrasonic measurements, *Bull. seism. Soc. Am.,* **104**(2), 931–943.

Winkler, K. W. & Murphy, W. F., III, 1995. Acoustic velocity and attenuation in porous rocks, in *Rock Physics and Phase Relations: A Handbook of Physical Constants,* pp. 20–34, ed. Ahrens, T.J., American Geophysical Union.

Zhu, T., Ajo-Franklin, J. B. & Daley, T. M., 2017. Spatiotemporal changes of seismic attenuation caused by injected CO_2 at the Frio-II pilot site, Dayton, TX, USA, *J. geophys. Res.,* **122**, 7156–7171.

Zhu, T., Ajo-Franklin, J. B., Daley, T. M. & Marone, C., 2019. Dynamics of geologic CO_2 storage and plume motion revealed by seismic coda waves, *Proc. Natl. Acad. Sci.,* **116**(7), 2464–2469.

SUPPORTING INFORMATION

Supplementary data are available at *GJI* online.

Figure S1. Example of the determination of Q_C estimates from the amplitude decay of a UT-signal. (a) From each moving window of the octave-width frequency filtered signal the (b) power spectral density (PSD) is estimated (black curve) and compared to the reference noise signal (blue curve). The red dots indicate measured coda amplitudes in the frequency domain. The insert shows the regression analysis of the amplitude decay. The largest amplitude measure (marked with the dark circle) belongs to the early coda portion (dark colour-coded window in (a)). The lowest amplitude measure (marked with the light circle) belongs to the late coda portion (light colour-coded window in (a)) Q_C estimates are calculated from the slope of the PSD regression line (black). (c) Final Q_C estimates (red dots) for each centre frequency of selected octave-width frequency bands are shown with error bars (σ_{Qc}). The spectral amplitudes of coda signal (black line) and reference noise (blue line) are shown in the background of which the SNR for each frequency band is calculated.

Figure S2. Visualization of UT groups (a) UT1$_{BH10\text{-}BEF}$ and UT3$_{BH10\text{-}BEF}$, and (b) UT10$_{BH12\text{-}AFT}$ and UT16$_{BH12\text{-}AFT}$ in boreholes BH10 and BH12, respectively, with approximated average ray paths (red and green lines) to the AE sensors. True sampled areas (ellipsoids) between source and receiver sampled by coda waves are not shown here. UT groups are marked with black dots. Shown rays run from the centre position of a UT group. The white dots indicate further UT-source points not considered in this manuscript. The yellow dots highlight damage zone markers from borehole televiewer logs.

Figure S3. Mean Q_C estimates from selected centre frequencies of octave-width frequency bands plotted with distance from centre of UT groups (a) UT1$_{BH10\text{-}BEF}$ and (b) UT3$_{BH10\text{-}BEF}$ to AE sensors. The symbols present selected centre frequencies (3, 10, 15 and 20 kHz). The colours indicate sensors along the driftway (magenta) and vein drift (turquoise). Error bars indicate the 2σ standard deviation (σ_{Qc}). The insert shows map view of the mine with centre of UT group (star) and average seismic ray path to sensors along the driftway (magenta lines) and vein drift (turquoise lines). The horizontal line at $Q_C = 140$ serves as a reference line across all plots.

Figure S4. Mean Q_C estimates from selected centre frequencies of octave-width frequency bands estimated at each AE sensor and plotted against azimuthal angle from groups (a) UT1$_{BH10\text{-}BEF}$ and (b) UT3$_{BH10\text{-}BEF}$. The colours indicate sensors along the driftway (magenta) and vein drift (turquoise). The symbols present selected centre frequencies (3, 10, 15 and 20 kHz). Error bars indicate the 2σ standard deviation (σ_{Qc}). The horizontal line at $Q_C = 140$ serves as a reference line across all plots.

Figure S5. Mean Q_C estimates from selected centre frequencies of octave-width frequency bands plotted with distance from centre of UT groups (a) UT1$_{BH10\text{-}AFT}$ and (b) UT1$_{BH16\text{-}AFT}$ to AE sensors. The symbols present selected centre frequencies (3, 10, 15 and 20 kHz). The colours indicate sensors along the driftway (magenta) and vein drift (turquoise). Error bars indicate the 2σ standard deviation (σ_{Qc}). The insert shows map view of the mine with centre of UT group (star) and average seismic ray path to sensors along the driftway (magenta lines) and vein drift (turquoise lines). The horizontal line at $Q_C = 140$ serves as a reference line across all plots.

Figure S6. Mean Q_C estimates from selected centre frequencies of octave-width frequency bands estimated at each AE sensor and plotted against azimuthal angle from groups (a) UT1$_{BH10\text{-}AFT}$ and (b) UT1$_{BH16\text{-}AFT}$. The colours indicate sensors along the driftway (magenta) and vein drift (turquoise). The symbols present selected centre frequencies (3, 10, 15 and 20 kHz). Error bars indicate the 2σ standard deviation (σ_{Qc}). The horizontal line at $Q_C = 140$ serves as a reference line across all plots.

Figure S7. Mean Q_C estimates from selected centre frequencies of octave-width frequency bands plotted with distance from centre of UT groups (a) UT10$_{BH12\text{-}AFT}$ and (b) UT16$_{BH12\text{-}AFT}$ to AE sensors. The symbols present selected centre frequencies (3, 10, 15 and 20 kHz). The colours indicate sensors along the driftway (magenta) and vein drift (turquoise). Error bars indicate the 2σ standard deviation (σ_{Qc}). The insert shows map view of the mine with centre of UT group (star) and average seismic ray path to sensors along the driftway (magenta lines) and vein drift (turquoise lines). The horizontal line at $Q_C = 140$ serves as a reference line across all plots.

Figure S8. Mean Q_C estimates from selected centre frequencies of octave-width frequency bands estimated at each AE sensor and plotted against azimuthal angle from groups a) UT10$_{BH12\text{-}AFT}$ and b) UT16$_{BH12\text{-}AFT}$. The colours indicate sensors along the driftway (magenta) and vein drift (turquoise). The symbols present selected centre frequencies (3, 10, 15 and 20 kHz). Error bars indicate the 2σ standard deviation (σ_{Qc}). The horizontal line at $Q_C = 140$ serves as a reference line across all plots.

Figure S9. Mean Q_C estimates from all AE sensors (symbols) for each analysed UT group (a–e) with slope n (blue line) which was fitted based on the frequency-dependent power law in equation (6).

Figure S10. Map view of the 40 m $\times$ 50 m $\times$ 30 m rock volume in the URL-RZ mine (Germany) showing assumed damage zone (red highlighted plane), location of injection interval shots and AE clouds with highest AE activities. Orientation and position of the damage zone is based on observations from borehole televiewer logs, structural markers along the walls of the galleries and the analysis of *S*-coda waves of UT measurements at deep and shallow depth intervals in boreholes BH10, BH16 and BH12.

Please note: Oxford University Press is not responsible for the content or functionality of any supporting materials supplied by the authors. Any queries (other than missing material) should be directed to the corresponding author for the paper.